

The Nature of Oxide Films on Tungsten in Acidic and Alkaline Solutions

R.S. Lillard, G.S. Kanner, D.P. Butt

Materials Corrosion and Environmental Effects Laboratory

Materials Science and Technology Division

Los Alamos National Laboratory

Los Alamos, NM 87545

Abstract

Surface enhanced Raman spectroscopy (SERS) data of W in acidic solution were characterized by modes associated with hydration ($\text{WO}_3(\text{H}_2\text{O})_x$, 942 cm^{-1}) as well as modes characteristic of WO_3 (816 cm^{-1}). At applied anodic potentials the $\text{WO}_3(\text{H}_2\text{O})_x$ content in the oxide was greater than the WO_3 content, while at applied cathodic potentials the WO_3 content was larger. These results are consistent with a bi-layer film on W in acidic solution which consists of a compact inner layer of WO_3 and an outer layer of $\text{WO}_3(\text{H}_2\text{O})_x$. Rotating disk electrode experiments (RDE) demonstrated that the passive dissolution (i_{pass}) of W in acidic solution increased with the angular velocity of the electrode. An increase in i_{pass} and a corresponding decrease in the thickness of the surface layer with increasing angular velocity is consistent with a reversible dissolution mechanism where dissolution is limited by the mass transport of a loosely bound $\text{WO}_3(\text{H}_2\text{O})_x$ layer from the surface. Electrochemical impedance spectroscopy measurements found that W dissolution in acidic solution was associated with an adsorption pseudocapacitance presumably due to the outer $\text{WO}_3(\text{H}_2\text{O})_x$ layer. The value of this pseudocapacitance increased with increasing angular velocity indicating thinning of the layer consistent with RDE and SERS results. Results for W in alkaline solution are also presented.

Introduction

Thermodynamically, tungsten trioxide (WO_3) is reported to be stable in acidic environments(1). However, the relatively high dissolution rate of WO_3 in acidic solution has long been recognized by those investigating the mechanism of WO_3 coloration (electrochromism) for application in the flat panel display industry(2). To date the exact mechanism by which this dissolution process occurs remains elusive. While in alkaline environments the dissolution of WO_3 is both thermodynamically favorable and experimentally observed, there has been no general agreement on the dissolution mechanism. The present study has focused on the role of the native oxide in the dissolution mechanism of tungsten in both acidic and alkaline environments. To examine oxide composition, structure, and hydration as a function of solution pH and applied potential *in situ*, surface enhanced Raman spectroscopy (SERS)(3) was employed. In addition, electrochemical impedance spectroscopy (EIS)(4, 5, 6) was used in conjunction with rotating disk electrode (RDE) experiments to examine the effects of mass transport on the native tungsten oxides as a function of solution pH and applied potential.

Background

Tungsten Electrochemistry While there have been several investigations of the anodic dissolution of W in alkaline solutions(7, 8, 9) the exact reaction mechanism is not widely agreed upon. Armstrong, Edmondson, and Firman studied the dissolution process for W in alkaline sodium hydroxide and sodium carbonate solutions(10). In this study, the stoichiometry of the reversible dissolution reaction was determined to be:



It was also recognized that the WO_3 surface species may take the form of $\text{WO}_3(\text{H}_2\text{O})_{\text{surface}}$. It was theorized that dissolution of WO_3 in alkaline solution was followed by a much slower reaction to the more thermodynamically stable species:



In a later study, Kelsey(11) demonstrated that the W dissolution reaction mechanism has a first order dependence on hydroxyl (OH⁻) concentration.

There have also been a number of studies of W dissolution in acidic environments. El-Basouney *et al.* concluded that the dissolution of WO₃ in acidic media occurs via the formation of a WO₂⁺² surface species(12, 13). Johnson and Wu, used open circuit potential (OCP) and potentiostatic polarization measurements to correlate tungsten electrode potentials in acid with regions of thermodynamic stability for various tungsten oxides(7). In these studies Johnson qualitatively determined that, when placed in acidic solution, W forms a protective oxide, presumably W₂O₅. Upon anodic polarization W₂O₅ was believed to be oxidized to WO₃. In addition, Johnson and Wu speculated that the dissolution process in acidic solution occurred via the hydration of WO₃ to WO₃(H₂O). In a more thorough study, Reichman and Bard described the kinetics of the electrochromic process (coloration of WO₃ oxides) in acidic media(2). They used cyclic voltametry and infrared spectroscopy to demonstrate that the water content of WO₃ films (for both anodically formed and evaporated oxides) increased with increasing number of anodic/cathodic potential cycles in acidic solution. Moreover they showed that the electrochromic process was enhanced in those films with the highest water content.

More recently, Macdonald *et al.* have characterized oxide film growth on tungsten in acidic solutions(14, 15, 16). In these studies, Mott-Schottky analysis of the passive film on tungsten was used to examine defect structure. To examine electronic state, photoelectrochemical impedance spectroscopy was employed. It was shown that passive film growth occurred at a rate of approximately 22 è /V. Correspondingly, the donor density within the vicinity of the metal/film interface (electron donors, presumably oxygen vacancies) decreased with increasing voltage. These results were rationalized in terms of the Point Defect Model(17). Specifically, the PDM predicts that cation vacancies are produced at the film / solution interface, then diffuse to and are annihilated at the metal / film interface while oxygen vacancies that are formed at the metal / film interface diffuse to and are consumed at the film / solution interface.

Surface Enhanced Raman Spectroscopy Traditional Raman spectroscopy has been used successfully to characterize the coloration process in WO_3 (18). In these experiments hydrated films of amorphous tungsten oxide (1500 \AA) were deposited onto aluminum substrates. After several anodic/cathodic potential cycles in acidic solution, the Raman spectra of these films were characterized by peaks in the 950 cm^{-1} region of the Raman spectrum consistent with $\text{WO}_3(\text{H}_2\text{O})_x$ formation

Because the intensity of Raman signals are inherently weak (*i.e.*, "bulk concentrations" are typically required), traditional Raman spectroscopy is not suitable for analyzing the thin oxides formed on W, as these films are generally less than 10 nm in thickness. However, researchers investigating adsorption of thin layers on metals found that gold substrates enhanced the Raman signal from adsorbates even for those layers which were only a few monolayers in thickness(19, 20). The origin of this enhancement is still a subject of controversy, but has been attributed to either chemical(21) or electromagnetic effects(22) and has been named surface enhanced Raman spectroscopy, or SERS.

More recently, investigators have found that the electrodeposition of discontinuous silver(3, 23, 24, 25) or gold(26) spheres (less than 50 nm in diameter) onto the native oxides formed on Ni and Fe electrodes also produced a Raman enhancing effect. Because the passive oxide produces a unique signal which is related to hydration, structure (*i.e.* co-ordination of atoms), and composition the SERS signal from a passive film is easily separated from Raman scattering owing to solution. SERS studies have demonstrated that the passive film on Ni was an amorphous hydrated oxide (presumably $\text{Ni}(\text{OH})_2$)(26), while passive Fe is covered by a mixed Fe_3O_4 and $\text{-Fe}_2\text{O}_3$ oxide(3, 27, 28).

Experimental

The samples evaluated in this study were fabricated from 99.96 at% tungsten. After making the electrical contact, each sample was mounted in epoxy and ground with successively finer grits of SiC paper and finished with alumina on a polishing wheel. The final mechanical polish being 0.3 μm alumina. In some cases this was followed by a chemi-mechanical polish with colloidal silica (0.06 μm , pH=10).

The solutions used in this investigation were: 1) sulfuric acid (pH 1.6), 2) 0.50 molar (M) boric acid / 0.05 M sodium borate (pH 7.2), and 3) 0.25 M sodium borate / sodium hydroxide (pH 10.6). All solutions were made with reagent grade chemicals and deionized water. As noted in the text, some solutions were deaerated with ultra high purity argon for 18 hours prior to immersion of the sample while others were bubbled with laboratory air. To eliminate chloride contamination, a mercury / mercury sulfate reference electrode (MMSE; +0.640V vs. normal hydrogen electrode (NHE)) was used. For the sake of clarity, all potentials are referenced vs. saturated calomel electrode (SCE, +0.241 vs. NHE).

Potentiodynamic polarization curves were generated at a scan rate of 0.1 mV/s in the potential region between -0.100 V vs. OCP and approximately +1.4 V vs. SCE. These curves were generated after 1 hour at the OCP to allow steady state to be achieved. EIS data were generated both at the OCP and at applied anodic potentials over the frequency range of 1×10^4 to 1×10^{-3} Hz. Data at applied anodic potentials were taken only after the current reached steady state (approximately 20 to 60 minutes). RDE experiments were carried out at rotation rates from 50 to 2000 revolutions per minute (rpm).

Surface Enhanced Raman experiments were performed with an Ar⁺ pumped Ti sapphire laser. Excitation was at 715 nm with an average power of approximately 50×10^{-3} watts and a focused spot diameter of approximately 200 μm . The incident light formed a 60° angle with the normal of sample surface. The scattered light was also collected at this angle. Data were collected over the range of 200 to 1200 cm^{-1} and calibrated with respect to the neon line spectrum. A liquid

cooled 298 x 1152 pixel CCD coupled to a 1/4 m spectrometer was used for detection giving 1152 points per scan. Although the data collection parameters varied slightly, a typical SER spectrum was obtained by averaging ten, 60-second scans. Prior to the SERS experiments a thin, discontinuous layer of gold spheres measuring approximately 50 nm in diameter (Figure 1) was potentiostatically electrodeposited at -0.90 V SCE onto each sample surface from a quiescent 5×10^{-4} M AuCl_3 solution. Approximately 30×10^{-3} Coulombs/cm² of charge was passed during each plating operation. Using a greater charge density resulted in columnar growth of the Au and little to no SERS enhancement. As in the EIS experiments, SERS data at applied anodic and cathodic potentials were taken only after the current reached steady state.

Results

SERS of W in Air and Deionized Water To examine the composition and structure of the native oxides and surface species which form on W, SERS was employed. In these experiments, Au was electrodeposited onto the W electrode to be examined in the manner discussed above. This layer was not found to alter the potentiodynamic polarization curves for W (not shown) which is consistent with other SERS investigations for iron and nickel (27, 28, 29). The SER spectra for a W electrode in air and in deionized / deaerated water are presented in Figure 2. Both spectra are identical in shape, characterized by several overlapping bands in the 600 to 1000 cm⁻¹ region of the plot.

An additional SER spectrum of the oxide formed on W in air is presented in Figure 3. In this figure the region of measurement has been extended to 200 cm⁻¹. Curve fitting analysis of these data finds that the SER spectrum for the native oxide on W was characterized by as many as 8 modes in the 200 to 1000 cm⁻¹ region. The approximate position of each mode is shown. Statistical analysis of the peak positions in the 700 to 1000 cm⁻¹ region from six SER spectra found modes at 942 ± 7 cm⁻¹, 897 ± 10 cm⁻¹, 816 ± 6 cm⁻¹, and 718 ± 6 cm⁻¹. The band at 942 cm⁻¹ is assigned to the A_g phonons of the $\text{WO}_3(\text{H}_2\text{O})_x$ lattice as observed by other investigators (30, 31, 32, 33). An example of this mode in $\text{WO}_3(\text{H}_2\text{O})$ is presented in Figure 4. In this figure the

traditional Raman spectra, measured with the 514.5 nm line of an Ar ion laser, for powders of WO_3 and $\text{WO}_3(\text{H}_2\text{O})$ (tungstite) are presented. In the case of tungstite, the unit cell of the orthorhombic crystal consists of four distorted octahedra(34). One of the axial oxygen positions in the octhedra can be occupied by a structural water molecule (Figure 5). This oxygen is associated with a much longer single bond than the opposite axial oxygen which forms the $\text{W}=\text{O}$ double bond (referred to as the terminal bond) and is associated with a mode at 943 cm^{-1} . The band at 376 cm^{-1} is linked to the stretch of the $\text{W}-\text{OH}_2$ (30) while the broad asymmetric band peaking at 630 cm^{-1} is probably associated with stretching motions within the equatorial plane.

The modes at 816 and 718 cm^{-1} in the SER spectrum for W in air have been assigned to the A_g phonons of the WO_3 lattice (Figure 4). The unit cell of the WO_3 crystal consists of eight corner sharing distorted and tilted WO_3 octahedra which form the unit cell(33, 35, 36). The bands at 253 and 334 cm^{-1} observed in the SER spectrum are likely associated with bending or deformation motions of the O-W-O equatorial bonds within the octhedra of crystalline WO_3 . Literature values for these Raman modes are 267 and 330 cm^{-1} (30, 33).

In order to check the symmetry of the modes in the SER spectrum, we have measured the effect of polarized light on the bands in the region from 600 to 1000 cm^{-1} . Using a polarization analyzer, the portions of the scattered light beam polarized parallel (I_{\parallel}) and perpendicular (I_{\perp}) to the incident beam were observed. The depolarization ratio $\rho = I_{\perp}/I_{\parallel}$ for the standard CCl_4 was measured and gave $\rho = 0.02$ for the A_g symmetry mode, in agreement with the accepted value for that band (37). In general, polarized bands, which can arise only from totally symmetric modes, exhibit $\rho = 0$ to 0.75 , whereas unpolarized modes will give $\rho = 0.75$. Figure 6 shows the optically polarized SER spectra for W coated with silver (Ag) spheres. The lineshapes are similar to what we observed for Au-coated W, but are redshifted by about 35 cm^{-1} . This shift may indicate that the dominant mechanism for the surface enhancement of the tungsten oxide modes is charge transfer between the oxide and the Au or Ag coating, which mediates the force constants that determine the

frequencies of vibration. We find that 0.4 0.6 across the spectral region from 650 to 950 cm^{-1} . This agrees with the A_g symmetry assignments of the 718 and 816 cm^{-1} modes for monoclinic WO_3 (37) and shows that the bands at 897 and 943 cm^{-1} are due to totally symmetric modes that we attribute to the hydrate.

While the origin of the band at 897 cm^{-1} is not entirely understood, a band at approximately 885 cm^{-1} has been measured by Aveston in the Raman spectrum of crystalline $\text{Na}_{10}\text{W}_{12}\text{O}_{41}(\text{H}_2\text{O})_{28}$.(38).

To summarize, the SER spectrum of the air formed oxide on W in the range of 700 to 1000 cm^{-1} was characterized by modes at approximately 942, 897, 816, and 718 cm^{-1} . For each of these modes in the SER spectra, there exists a corresponding mode in the traditional Raman spectra of either WO_3 or $\text{WO}_3(\text{H}_2\text{O})$ powders. From these results it may be concluded that the air formed oxide on W contains both WO_3 (possibly crystalline) and $\text{WO}_3(\text{H}_2\text{O})_x$.

SERS of W in Acidic Environment Representative SER spectra for W in pH 1.6, sulfuric acid (ambient aeration) as a function of applied cathodic potential are presented in Figure 7. For comparison the SER spectrum for W in air (measured just prior to immersion in solution) is also presented in this figure. In each of the *in situ* spectra, the small sharp peak at approximately 982 cm^{-1} owes to the sulfuric acid solution and is not associated with W or its oxides(39). While an arbitrary value was added to each spectrum for clarity of presentation, no multiplication factor was used. Thus, the relative peak intensities in Figure 7 can be compared. To aid in identification of peak positions, reference lines at 900, 800, 350, and 200 cm^{-1} have been added to the plot. Each of the applied potentials used in this experiment represent a different region of the Pourbaix diagram as shown in Figure 8. As seen in Figure 7, the SER spectrum taken in solution at the OCP (+0.02 V SCE) was similar in shape to the SER spectrum for W in air although the intensity of the scattered light is much greater.

After the SERS data were acquired at the OCP, the sample was cathodically polarized to -0.51 V SCE. While this potential is 0.055 V more negative than the W reduction potential at this pH (Figure 8), no indication of the reduction of W oxide was found in this SER spectrum.

Moreover, the signal-to-noise ratio at -0.510 V SCE was greater than that measured at the OCP. A Gaussian curve fit of the SERS data taken at -0.51 V is presented in Figure 9. As seen in this figure, a one-to-one correspondence between the fitted peaks at -0.510 V and the fitted peaks in air (Figure 3) was found. What appears to be a shift in the position of SERS peaks in the 900 cm^{-1} region of the plot in Figure 7 is explained as a change in the relative heights of the 943, 899, and 803 cm^{-1} peaks. Analysis of the relative peak heights as a function of applied potential is presented later in this paper.

After polarization at -0.51 V SCE for approximately 1 hour, the W electrode potential was stepped to more positive potentials and additional SER spectra were measured. At -0.39 V SCE, the SER spectrum for W was characterized by peaks at the same positions noted in the -0.51 V spectra. However, the ratio of the relative peak heights in the 700 to 1000 cm^{-1} and 200 to 500 cm^{-1} regions of the plot changed. Thermodynamically, this potential is in a region of WO_2 stability (Figure 8). Following polarization at -0.390 V, the applied potential was stepped to -0.200 V SCE. Thermodynamically, this potential is in a region of WO_3 stability (Figure 8). At -0.200 V SCE, the SER spectrum for W was characterized by peaks at the same positions noted in the -0.390 V spectra indicating that no change in the crystal structure and, therefore, no change in the oxidation state of the oxide film occurred in stepping the potential from -0.51 V to -0.39 V or from -0.39 V to -0.20 V.

Typical SER spectra for W in H_2SO_4 as a function of applied anodic potential are presented in Figure 10. Once again an arbitrary value was added to each spectrum for clarity of presentation, and reference lines at 900, 800, 350, and 200 cm^{-1} are also shown in this figure. The shifting of the composite peak in the 912 cm^{-1} region of the plot is again explained by a change in the relative heights of the 942, 897, and 816 cm^{-1} peaks. A plot of the ratio of the 942, 897, and 816 cm^{-1} peak heights as a function of applied potential is presented in Figure 11. As seen in this figure the relative height of the peak associated with $\text{WO}_3(\text{H}_2\text{O})_x$ (942 cm^{-1}) is maximum at applied anodic potentials. In contrast, the peak associated with WO_3 (897 cm^{-1}) is maximum at applied cathodic potentials. From this result it may be concluded that the anodic polarization of W in acidic solution

is associated with an increase in the $\text{WO}_3(\text{H}_2\text{O})_x$ content while at applied cathodic potentials, the WO_3 content is increased. Other Raman investigations of thin film W oxides ($\text{WO}_3(\text{H}_2\text{O})_{1.74}$), have shown that dehydration was characterized by a decrease in the 950 cm^{-1} mode and a corresponding enhancement in the bands located in the 600 to 900 cm^{-1} region(40).

SERS of W in Alkaline Environment Typical SER spectra for W in pH 10.6 solution as a function of potential are presented in Figure 12. Raman modes from the solution were observed at approximately 725 cm^{-1} as noted in this figure. The SERS data for W in base at the OCP are characterized by 10-12 Raman modes: 4 modes in the 1000 to 1200 cm^{-1} region, 1 mode at 937 cm^{-1} and 5 to 6 modes in the 410 to 590 cm^{-1} region. No bands at 897 , 816 , and 718 cm^{-1} appear in the SER spectrum of W in alkaline solution. In addition, the band at 937 cm^{-1} is not the primary mode in this spectra (as indicated by its relative height). For this reason it is likely that this peak is not associated with a shifting of the A_g phonons in $\text{WO}_3(\text{H}_2\text{O})_x$ lattice observed at 943 cm^{-1} in the SER spectra for W in sulfuric acid above. The origin of the SERS modes in the 410 to 590 cm^{-1} region and the 1000 to 1200 cm^{-1} regions are presently not understood. Currently no W oxide, compound, or ionic species is known to have fundamental vibrations in these regions.

At -1.1 V SCE , (63 mV more negative than the reduction potential at this pH) the band at 937 cm^{-1} is no longer observed. In addition, with the exception of the peaks observed in the 410 to 590 cm^{-1} region of the spectrum it appears that none of the bands observed at the OCP are present in the spectrum at -1.1 V SCE . Considering that this potential is in a region of W^0 thermodynamic stability and a decrease in the total number of peaks in the SER spectra was measured, it is reasonable to conclude that the oxide which forms on W in alkaline solution is at least partially reduced at cathodic potentials. Recall that reduction of the native oxide was not observed in pH 1.6 solution.

Due to rapid dissolution of W at applied anodic potentials in alkaline environment, reproducible SERS data were not obtained above the OCP.

Effects of Mass Transport Potentiodynamic polarization curves for W as a function of solution pH are presented in Figure 13. As can be seen in this figure, neutral and alkaline

solutions were associated with lower OCPs and higher anodic dissolution rates than observed in acidic solution. While the anodic current densities in the pH 1.6 solution were relatively low, they were an order of magnitude higher than those associated with the passivity of, for example, stainless steels, tantalum, or aluminum (41, 42, 43). However, the reverse scan for W in pH 1.6 was associated with a negative hysteresis and a more positive second OCP as observed in other passive metals and is attributed to oxide film growth.

The effects of mass transport on the passive dissolution rate were examined with the RDE technique. These experiments found that the passive current density (i_{pass}) in acidic solution was related to the angular velocity of the electrode. As seen in Figure 14, i_{pass} increased from 11 $\mu\text{A}/\text{cm}^2$ in the absence of rotation to approximately 82.5 $\mu\text{A}/\text{cm}^2$ at $\omega^{1/2} = 14.5$ (in radians/s). No increase in i_{pass} was observed at greater angular velocities. This phenomenon has also been observed for the Fe / H_2SO_4 and Fe/ H_3PO_4 systems(44). Keddam *et al.* found the increase in i_{pass} to be small for the Fe / H_2SO_4 system, changing only from 0.90 $\mu\text{A}/\text{cm}^2$ in quiescent solution to 0.99 $\mu\text{A}/\text{cm}^2$ for $\omega^{1/2} = 28.9$. At values of $\omega^{1/2}$ greater than 28.9, Keddam found no further increase in i_{pass} with increasing rotation rate. The relationship between the iron passive current density and angular velocity was attributed to the adsorption / desorption of a hematite film on the Fe surface. Here, for the W / H_2SO_4 system, the increase in i_{pass} with increasing ω is associated with the desorption of $\text{WO}_3(\text{H}_2\text{O})_x$ from the electrode surface. This layer exists as a loosely bound intermediate in the dissolution process and is in equilibrium with the diffusion boundary layer in a manner similar to that described for the passive film on iron(44).

EIS experiments for W in pH 1.6 sulfuric acid were performed at an applied anodic potential of 0.2 V SCE both with and without rotation (Figure 15). In quiescent solution the EIS data were characterized by two RC time constants. While the impedance data below 0.025 Hz may appear to follow the formula for diffusional impedance as expressed by Warburg: $Z_w = (j\omega)^{-1/2}$ (45, 46) (expressed in Figure 15 as a dashed line with slope = -1), an RC time constant gave a

better fit. This point may be seen more clearly during EIS-RDE experiments where the low frequency limit of the time constant was within the measured frequency range (Figure 15). This behavior was also observed both in neutral (Figure 16) and alkaline solutions, and has been attributed by other investigators to the adsorption phenomena(44).

The equivalent circuit (EC) used to model the adsorption phenomena is presented in Figure 17 (47, 48, 49) where: R_{ct} is the impedance associated with the charge transfer reaction, C_{dl} is the capacitance associated with the double layer, R_{as} represents the impedance associated with an adsorbed species that is in equilibrium with the diffusion boundary layer, and C_{as} is the capacitance associated with this adsorbed species (often referred to as an adsorption pseudocapacitance(50, 51). Here, the outer $WO_3(H_2O)_x$ layer (described in the SERS and RDE experiments above) is believed to give rise to the adsorption phenomenon for W in acidic solution. A typical complex non-linear least squares fit of the EC in Figure 17 to the EIS data is presented in Figure 18. As shown in this figure, good agreement between the EC model and the experimental data for W was observed. Values for R_{as} , C_{as} , R_{ct} , and C_{dl} from CNLS fits of the EIS data as a function of solution pH and rotation rate at an applied potential of 0.20 V are presented in Table 1. Table 1 demonstrates that for all solutions C_{as} increased with increasing angular velocity. An increase in C_{as} is equivalent to an decrease in the thickness of the adsorbed intermediate ($C = \epsilon A/d$, where d is thickness). While the values for the adsorption pseudocapacitance in Table 1 appear to be high compared to the capacitances associated with the double layer (10's of $\mu F/cm^2$), these values for C_{as} are of the same order of magnitude as those pseudocapacitances observed for hydrogen adsorption(52) and adsorbed Fe films on steel(51, 53). Although R_{as} and R_{ct} decreased during RDE experiments, in acidic solution the rate determining step for passive dissolution was always the $WO_3(H_2O)_x$ layer (i.e., R_{as} was always greater than R_{ct} in acidic solution). In alkaline solution, R_{as} decreased during RDE experiments to a value less than R_{ct} indicating that dissolution was controlled by the adsorbed species in quiescent solution and by charge transfer at an angular velocity of $\omega^{1/2} = 14.5$.

Discussion

The results of this investigation are consistent, in part, with the study of DiPaola *et al.*(54) who found that the oxide on tungsten formed during anodic polarization in acidic solution had both barrier and hydrated layers. In these studies, x-ray diffraction patterns from anodically formed thick films on W indicated the presence of H₂O(55). In our interpretation of this bi-layer film, the oxide formed on W is believed to consist of 1) a compact inner layer of WO₃ (possibly crystalline) and 2) an outer layer of WO₃(H₂O)_x, that is loosely bound. Moreover, the oxidation state of the native oxide is W(VI), independent of applied potential.

The dissolution mechanism for W in acidic solution is governed by the outer WO₃(H₂O)_x layer. In quiescent solution, anodic polarization results in the thickening of the hydrate layer as shown by the SERS data where the ratio of hydrate to WO₃ was found to be a function of applied potential: at applied anodic potential the fraction of oxide which exists as WO₃(H₂O)_x was maximized while at applied cathodic potentials the fraction of WO₃ was maximized. As the WO₃(H₂O)_x layer was determined to be the rate determining step in the dissolution mechanism (i.e. $R_{as} > R_{ct}$) a thicker WO₃(H₂O)_x layer explains the relatively low i_{pass} observed in the potentiodynamic polarization curves. In agitated solutions the hydrate layer thins, as demonstrated by an increase in the adsorption pseudocapacitance and decrease in R_{as} . As may be anticipated, this results in an increase in the dissolution rate (i. e. higher i_{pass}). Correspondingly, an increase in i_{pass} was observed with increasing ω . An increase in the passive dissolution rate with angular velocity is consistent with a reversible dissolution mechanism where dissolution is limited by the mass transport of a loosely bound hydrated layer from the electrode surface(10). These results for W in acidic solution are also consistent with the observation that hydrates of WO₃ are more soluble than the oxide itself(56). However, the mechanism by which hydration occurs in acidic solution is presently not understood. It is unclear if the increase in the ratio of WO₃ to WO₃(H₂O)_x during cathodic polarization owes to dehydration, as would be indicated by an oxide thickness which was independent of applied cathodic potential, or thinning of the WO₃(H₂O)_x layer.

In alkaline solution the EIS data could be modeled by the same EC used to describe W dissolution in acidic solution. In addition, i_{pass} and the adsorption pseudocapacitance (at an applied potential) increased with increasing angular velocity as they did in acidic solution. However, the SERS data clearly indicate that the dissolution mechanism in alkaline solution does not involve $\text{WO}_3(\text{H}_2\text{O})_x$ formation. Therefore, while the EIS model may describe how a surface species behaves, it in no way sheds light on the nature of the species on the W surface. Moreover, while the adsorption pseudocapacitance owes to the $\text{WO}_3(\text{H}_2\text{O})_x$ layer in acidic solution another species must be responsible for this parameter in alkaline solution.

Summary

The SER spectra for W in air and in acidic solution were dominated by three modes at approximately 816, 885, and 942 cm^{-1} . The modes at 816 and 942 cm^{-1} were associated with the A_g vibrational modes of WO_3 and $\text{WO}_3(\text{H}_2\text{O})_x$ respectively. Upon cathodic polarization of the W electrode in acidic solution, an increase in the 816 / 942 peak height ratio was observed indicating the oxide was becoming enriched in WO_3 . Upon anodic polarization of the W electrode in acidic solution, a decrease in the 816 / 942 peak height ratio was observed indicating the oxide was becoming enriched in $\text{WO}_3(\text{H}_2\text{O})_x$. In addition, the oxidation state of the native oxide is W(VI) independent of applied potential.

RDE experiments found that the passive current density for W in acidic solution increased with the angular velocity of the electrode. An increase in the passive dissolution rate with angular velocity is consistent with a reversible dissolution mechanism where dissolution is limited by the mass transport of a loosely bound $\text{WO}_3(\text{H}_2\text{O})_x$ layer from the electrode surface.

RDE-EIS experiments also demonstrated that the passive dissolution of W in acidic solution was limited by mass transport. In these experiments the passive dissolution process was associated with an adsorption pseudocapacitance owing to $\text{WO}_3(\text{H}_2\text{O})_x$. The value of this pseudocapacitance was found to increase with angular velocity indicating a decrease in the thickness of the $\text{WO}_3(\text{H}_2\text{O})_x$ layer. Moreover, EIS experiments demonstrated that the rate

determining step for the passive dissolution W in acidic was always the discharge of the adsorbed species.

From these results a theory describing the anodic dissolution of tungsten was formed. In this theory the oxide on W is believed to consist of 2 layers, an inner barrier layer of WO_3 and an outer hydrated layer consisting of $\text{WO}_3(\text{H}_2\text{O})_x$.

Acknowledgments

All work on this project was performed under the auspices of the University of California for the US department of Energy contract W-7405-ENG-36. The authors would like to thank Laurie Waters and the continued support of the APT project office, Doris Ford for some of the early polarization experiments, and Dave Kolman for helpful discussions.

References

1. M. Pourbaix, *Atlas of Electrochemical Equilibria*, NACE-Cebelcor, Houston (1974).
2. B. Reichhman and A. J. Bard, *The Journal of the Electrochemical Society*, **126**, 583 (1979).
3. J. Gui and T. M. Devine, *Corrosion Science*, **32**, 1105 (1991).
4. D. D. MacDonald and M. C. H. McKubre, in *ASTM STP 727, Electrochemical Corrosion Testing*, F. Mansfeld and U. Bertocci, Editors, p. 110, ASTM, Philadelphia (1981).
5. I. Epelboin, C. Gabrielli, M. Keddam, and H. Takenouti, in *ASTM STP 727, Electrochemical Corrosion Testing*, F. Mansfeld and U. Bertocci, Eds., p. 150, ASTM, Philadelphia (1981).
6. J. R. MacDonald, *Impedance Spectroscopy*, Wiley Publishing, New York (1987).
7. J. W. Johnson and C. L. Wu, *The Journal of the Electrochemical Society*, **118**, 1909 (1971).
8. P. I. Ortiz, M. L. Teijelo, and M. C. Giorano, *Journal of Electroanalytical Chemistry*, **243**, 379 (1988).
9. M. K. Thompson and C. W. Rice, *Transactions of the Electrochemical Society*, **67**, 71 (1935).
10. R. D. Armstrong, K. Edmondson, and R. E. Firman, *Journal of Electroanalytical Chemistry*, **40**, 19 (1972).
11. G. S. Kelsey, *The Journal of the Electrochemical Society*, **124**, 814 (1977).
12. M. S. El-Basiouny, F. E. T. Heakel, and M. M. Hefny, *Corrosion*, **37**, 175 (1981).
13. M. S. El-Basiouny, S. A. Hassan, and M. M. Hefny, *Corrosion Science*, **20**, 909 (1980).
14. D. D. Macdonald, S. R. Biaggio, and H. Song, *The Journal of the Electrochemical Society*, **139**, 170 (1992).
15. E. Sikora, J. Sikora, and D. D. MacDonald, *Electrochimica Acta*, **41**, 783 (1996).
16. E. Sikora and D. D. MacDonald, *Solid State Ionics*, **94**, 141 (1997).

17. D. D. MacDonald and M. Urquidi-MacDonald, *The Journal of the Electrochemical Society*, **137**, 2395 (1990).
18. M. F. Daniel, B. Desbat, J. C. Lassegues, and R. Garie, *Journal of Solid State Chemistry*, **73**, 127 (1988).
19. J. Desilvestro, D. A. Corrigan, and M. J. Weaver, *Journal of Physical Chemistry*, **90**, 6408 (1986).
20. M. Fleischmann, P. J. Hendra, and A. J. McQuillen, *Chemical Physics Letters*, **26**, 163 (1974).
21. A. Otto, J. Billman, J. Eikmans, U. Erturk, and C. Pettenkotter, *Surface Science*, **138**, 319 (1984).
22. M. Kerker, D. S. Wang, and H. Chew, *Applied Optics*, **19**, 4159 (1985).
23. M. G. S. Ferreira, T. Moura-e-Silva, A. Catarino, M. Pakuch, and C. A. Melendres, *The Journal of the Electrochemical Society*, **139**, 3146 (1992).
24. C. A. Melendres and M. Pankuch, *Journal of Electroanalytical Chemistry*, **333**, 103 (1992).
25. J. C. Rubim and J. Dunnwald, *Journal of Electroanalytical Chemistry*, **258**, 327 (1989).
26. L. J. Oblonsky and T. M. Devine, *The Journal of the Electrochemical Society*, **142**, 3677 (1995).
27. J. Gui and T. M. Devine, *The Journal of the Electrochemical Society*, **138**, 1376 (1991).
28. J. Gui and T. M. Devine, *Corrosion Science*, **36**, 441 (1994).
29. L. J. Oblonsky and T. M. Devine, *Corrosion Science*, **37**, 17 (1995).
30. M. F. Daniel, B. Desbat, J. C. Lassegues, B. Gerand, and M. Figlarz, *Journal of Solid State Chemistry*, **67**, 235 (1987).
31. I. V. Shiyankovskaya, T. A. Gavrilko, and E. V. Gabrusenoks, *Journal of Molecular Structure*, **293**, 295 (1993).
32. I. V. Shiyankovskaya, H. Ratajczak, J. Baran, and M. Marchewka, *Journal of Molecular Structure*, **348**, 99 (1995).

33. E. Salje, *Acta Crystallography*, **A31**, 360 (1975).
34. J. T. Szymanski and A. C. Roberts, *Canadian Minerologist*, **22**, 681 (1984).
35. B. O. Loopstra and P. Boldrini, *Acta Crystallography*, **21**, 158 (1966).
36. S. Tanisaki, *Japanese Physical Society*, **15**, 573 (1960).
37. K. Nakamoto, *Infrared and Raman Spectra of Inorganic and Coordination Compounds*, J. Wiley & Sons, New York (1978).
38. J. Aveston, *Inorganic Chemistry*, **3**, 981 (1964).
39. C. K. Ingold, D. J. Millen, and H. G. Poole, *Journal of the Chemical Society*, **106**, 2576 (1950).
40. G. M. Ramans, J. V. Gabrusenoks, and A. A. Veispals, *Physica Status Solidi (a)*, **74**, k41 (1982).
41. A. P. Bond, E. A. Lizlovs, H. J. Dundas, and A. Pozansky, in *Electrochemical Techniques for Corrosion Engineering*, R. Baboin, Editor, p. 127, NACE, Houston (1986).
42. G. D. Davis, B. A. Shaw, B. J. Rees, E. L. Principe, and C. A. Pecile, *Surface and Interface Analysis*, **23**, 609 (1993).
43. P. M. Natishan, E. McCafferty, and G. K. Hubler, *The Journal of the Electrochemical Society*, **135**, 321 (1988).
44. M. Keddam and C. Pallota, *The Journal of the Electrochemical Society*, **132**, 781 (1985).
45. D. C. Grahame, *The Journal of the Electrochemical Society*, **99**, 370C (1952).
46. J. E. B. Randles, *Discussion of the Faraday Society*, **1**, 11 (1947).
47. H. Gerisher, *Zeitschrift fur Physike Chemie*, **201**, 55 (1952).
48. R. D. Armstrong, M. F. Bell, and A. A. Metcalfe, *Electrochemistry - Specialist Periodical Reports*, **6**, 98 (1978).
49. R. D. Armstrong and M. Henderson, *Journal of Electroanalytical Chemistry*, **39**, 81 (1972).
50. E. Gileadi, *Electrode Kinetics for Chemists, Chemical Engineers, and Materials Scientists*, VCH Publishers Inc., New York (1993).

51. S. G. Ehrlich and P. J. Moran, *Corrosion*, **45**, 689 (1989).
52. B. E. Conway and E. Gileadi, *Transactions of the Faraday Society*, **58**, 2493 (1962).
53. J. N. Murray, P. J. Moran, and E. Gileadi, *Corrosion*, **44**, 533 (1987).
54. A. DiPaola, F. DiQuarto, and C. Sunseri, *Corrosion Science*, **20**, 1067 (1980).
55. A. DiPaola, F. DiQuarto, and C. Sunseri, *The Journal of the Electrochemical Society*, **125**, 1344 (1978).
56. N. N. Greenwood and A. Earnshaw, *Chemistry of the Elements*, Pergamon Press, Oxford (1984).

Table 1 EIS parameters from the EC presented in Figure 5 for W as a function of solution pH. All data were taken at an applied potential of +0.20 V SCE.

| pH | no rotation | | | RDE: $\omega^{1/2}=14.5$ | | |
|-------------|---------------------------------|---------------------------------|--------------------------------|---------------------------------|---------------------------------|--------------------------------|
| | R_{ct} ohm·cm ² | R_{as} ohm·cm ² | C_{as} μF/cm ² | R_{ct} ohm·cm ² | R_{as} ohm·cm ² | C_{as} μF/cm ² |
| 1.6 | 3530 | 2.14x10 ⁴ | 3400 | 1220 | 5550 | 7800 |
| 7.2 | 661 | 1.24x10 ⁴ | 8100 | 122 | 109 | 1.3 x10 ⁴ |
| 10.6 | 12 | 91 | 3.4 x10 ⁴ | 4 | 1 | 5.5 x10 ⁴ |

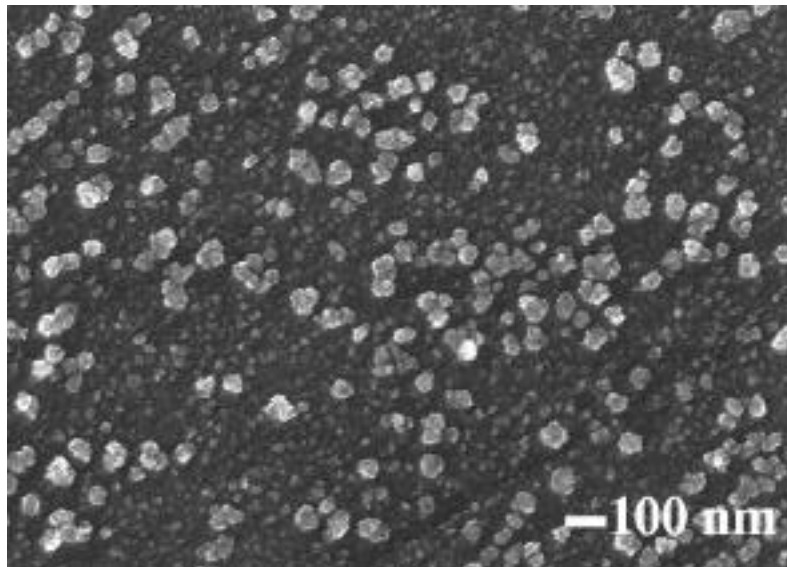


Figure 1 High resolution SEM micrograph of tungsten after electroplating process. Micrograph shows size and shape of gold spheres that produced SERS. It was noted that larger spheres and / or a columnar shape did not produce the Raman enhancing effect.

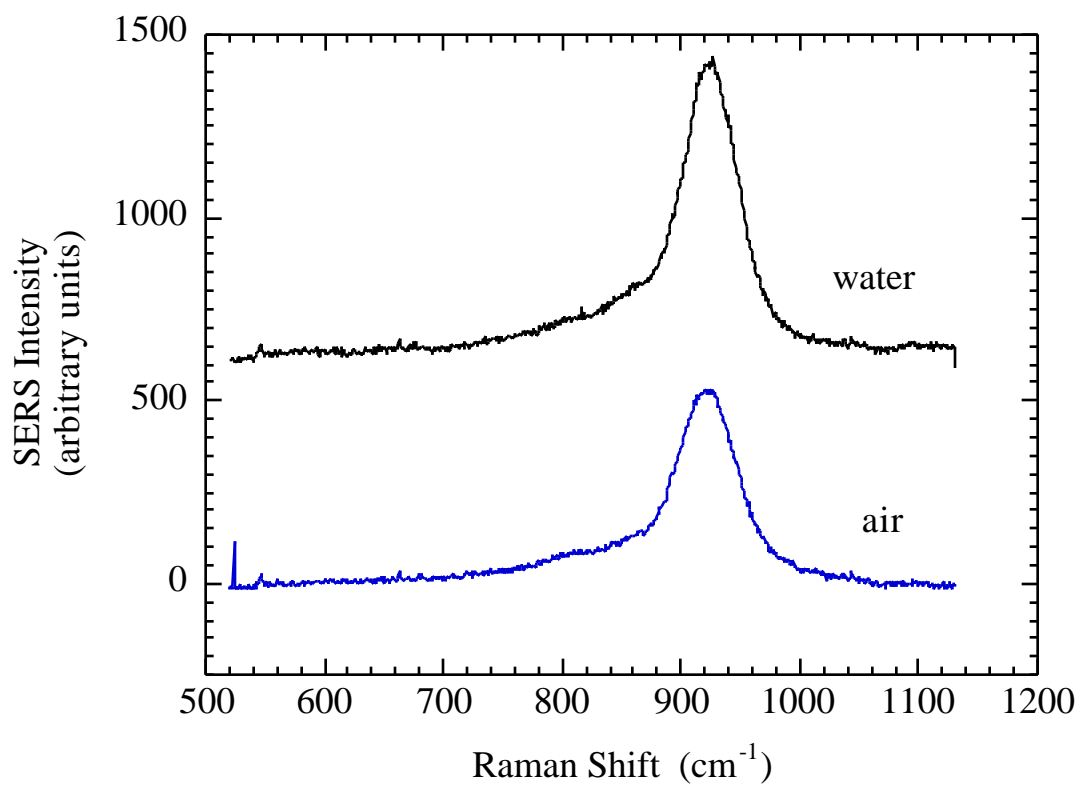


Figure 2 SERS spectra for W in air and in deionized water at the OCP (500 to 1100 cm⁻¹ region only).

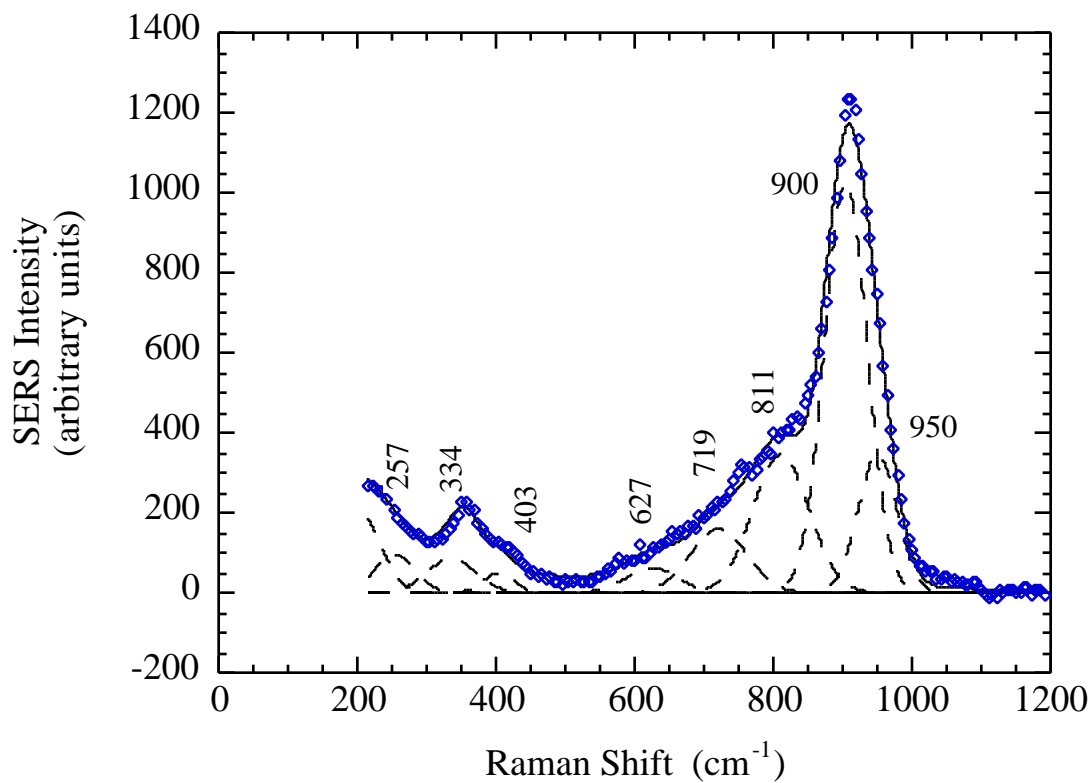


Figure 3 SERS spectra for W in air (background subtracted) and Gaussian curve fit. The experimental data (diamond), individual peaks (dashed line), peak positions in cm⁻¹, and sum-fit (solid line) are presented.

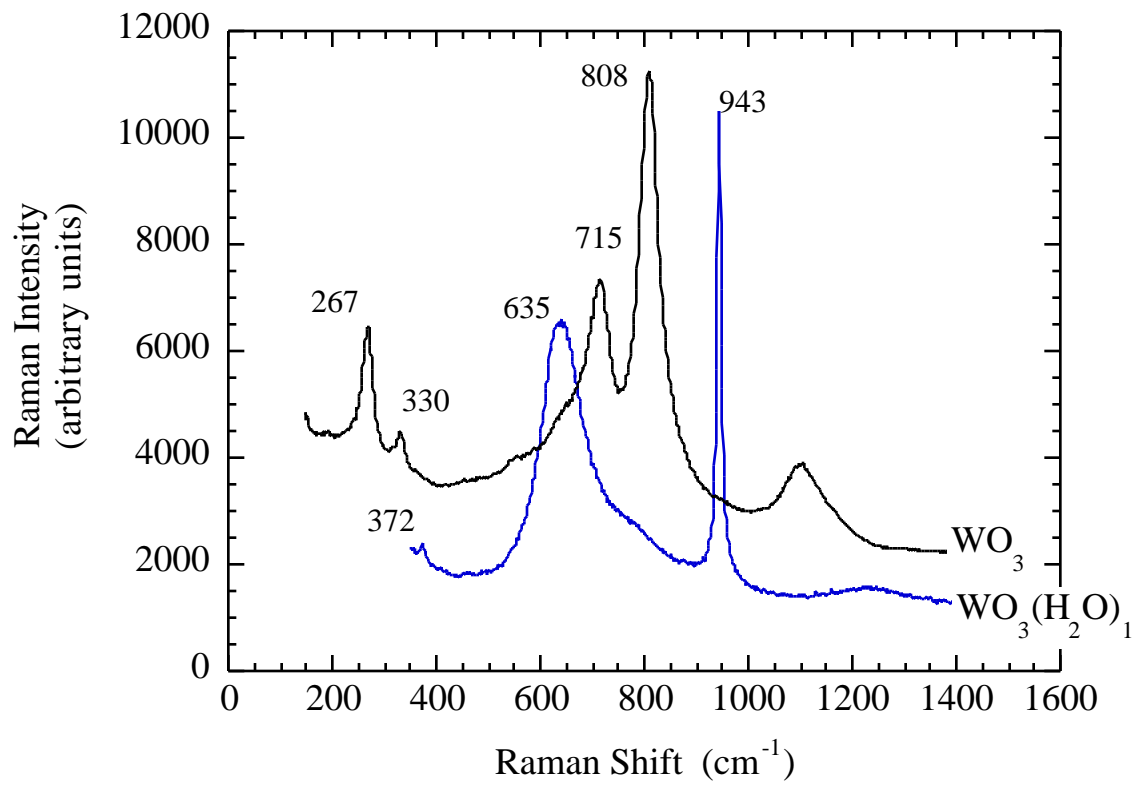


Figure 4 Raman spectra for powders of WO_3 and $\text{WO}_3(\text{H}_2\text{O})_1$. Approximate peak positions are also presented.

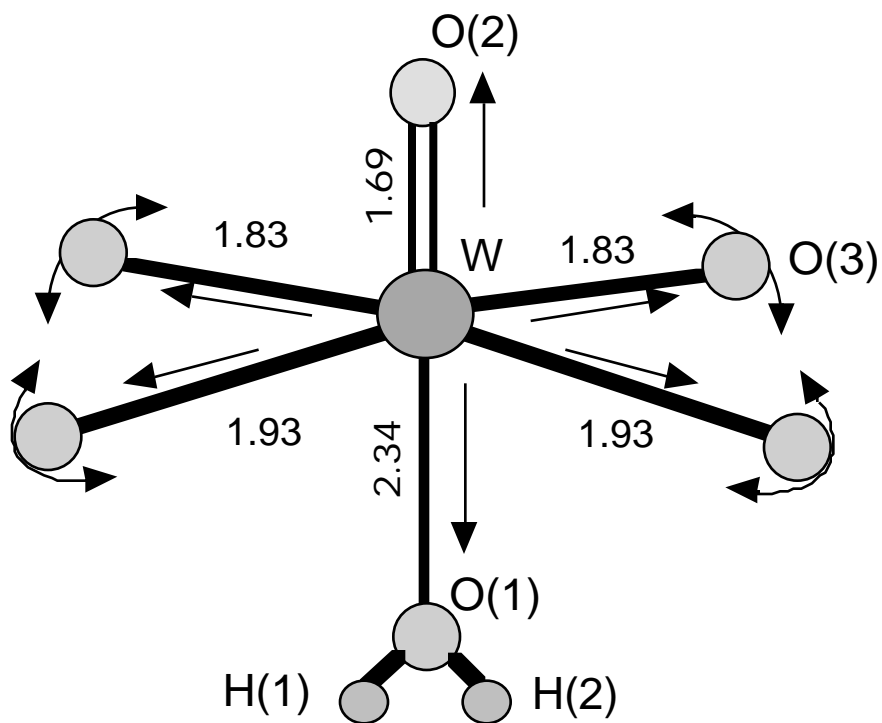


Figure 5 Diagram of one of the octahedra which exists in $\text{WO}_3(\text{H}_2\text{O})_x$. Approximate bond lengths and some of the many bending and stretching modes which are Raman active are also shown.

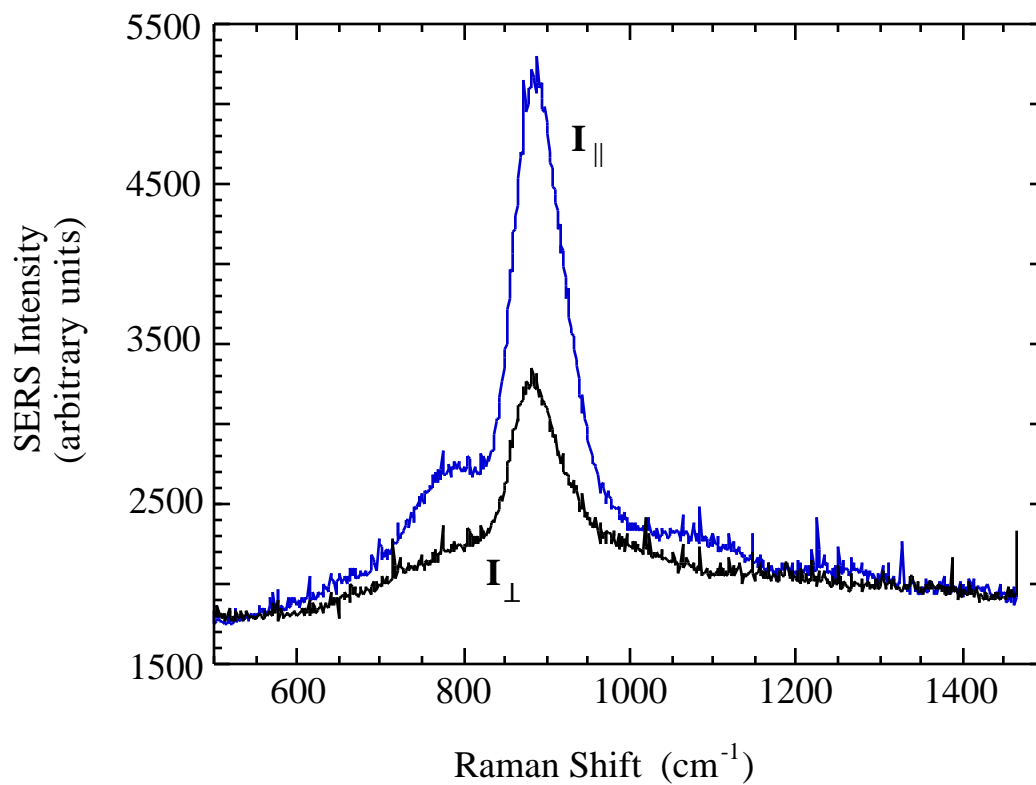


Figure 6 Optically polarized SERS spectra for tungsten in air. Figures shows both the horizontal component, I_{\parallel} , and the perpendicular component, I_{\perp} , of the scattered light (with respect to polarization of the incident beam).

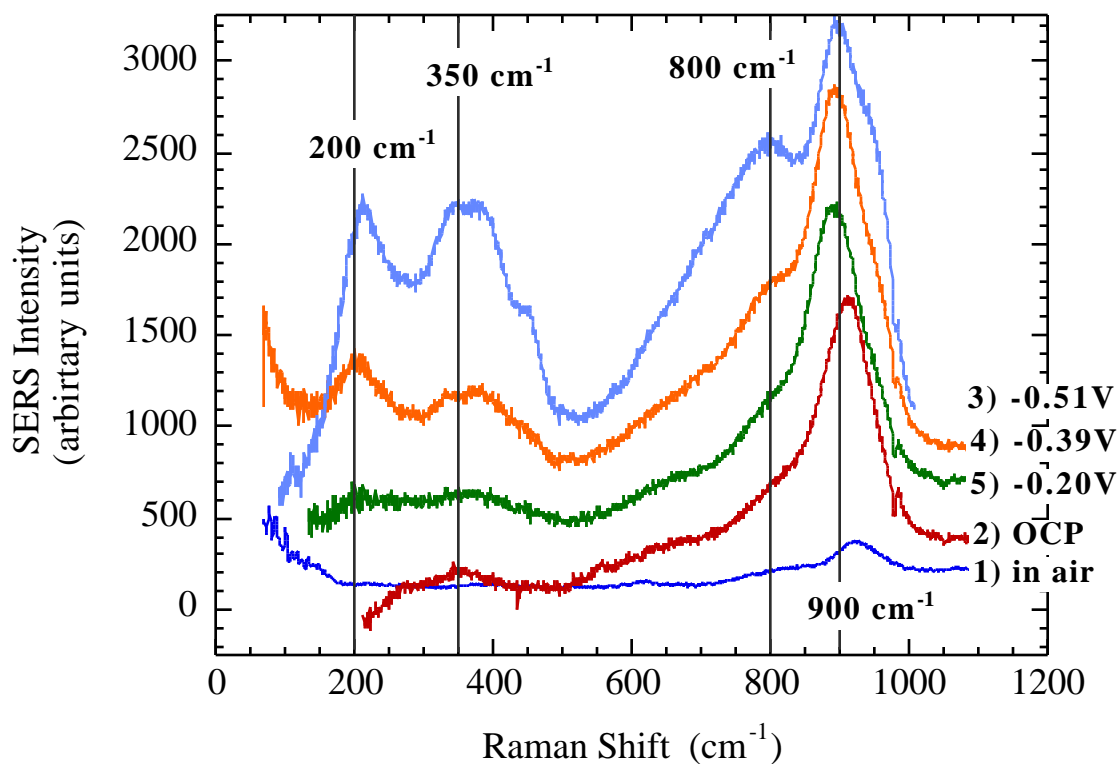


Figure 7 *In situ* SERS spectra of W as a function of applied cathodic potential. (pH 1.6 H₂SO₄). The number of each curve represents the order of experiments. The apparent shifting of the composite peak in the 912 cm⁻¹ region of the plot is explained as a change in relative peak heights of the 942, 897, and 816 cm⁻¹ peak heights.

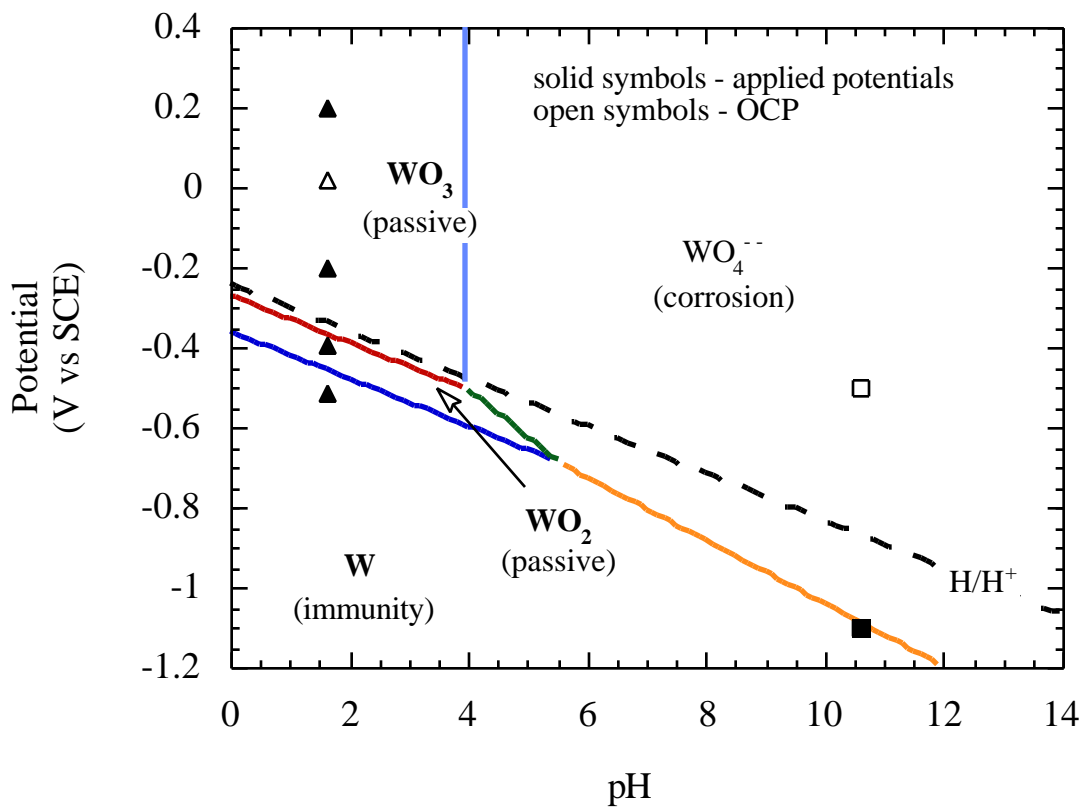


Figure 8 Pourbaix diagram for tungsten. This diagram was calculated for 10^{-6} M WO_4^{2-} . Plot also displays the potentials at which *in situ* SERS data were collected.

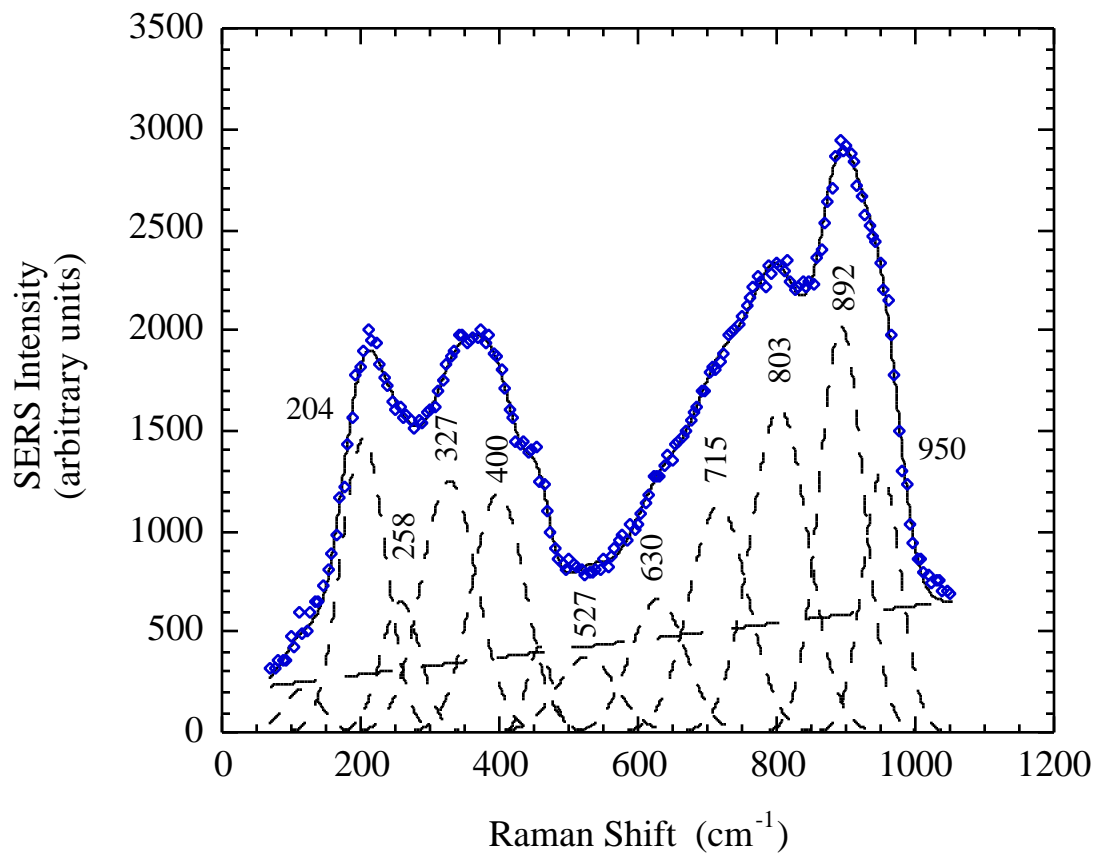


Figure 9 SERS spectra for W in H₂SO₄ pH 1.6 at -0.510 V vs. SCE and Gaussian curve fit. The experimental data (diamond), background (long dash), individual peaks (short dash), peak positions in cm⁻¹, and sum-fit (solid line) are present.

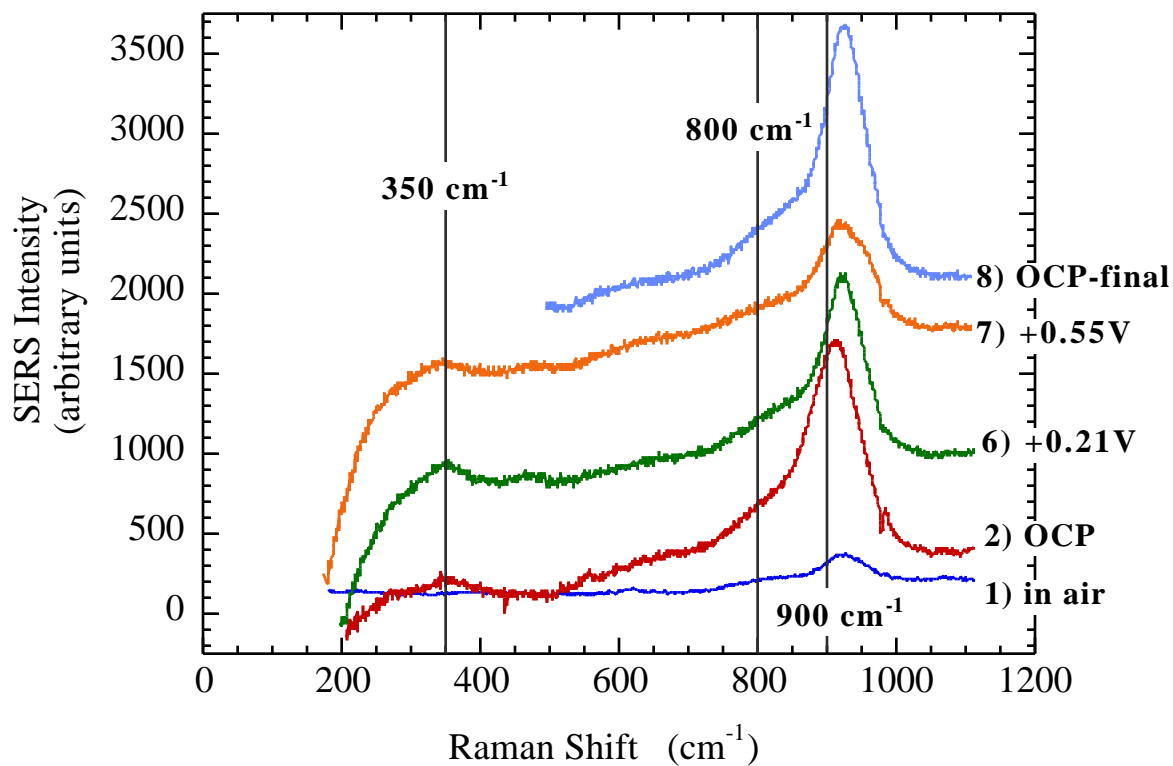


Figure 10 *In situ* SERS spectra of W as a function of applied anodic potential. (pH 1.6 H₂SO₄). In-air spectrum is also presented for reference. The number of each curve represents the order of experiments. Note, the anodic SERS experiments were conducted after the cathodic experiments (Figure 7).

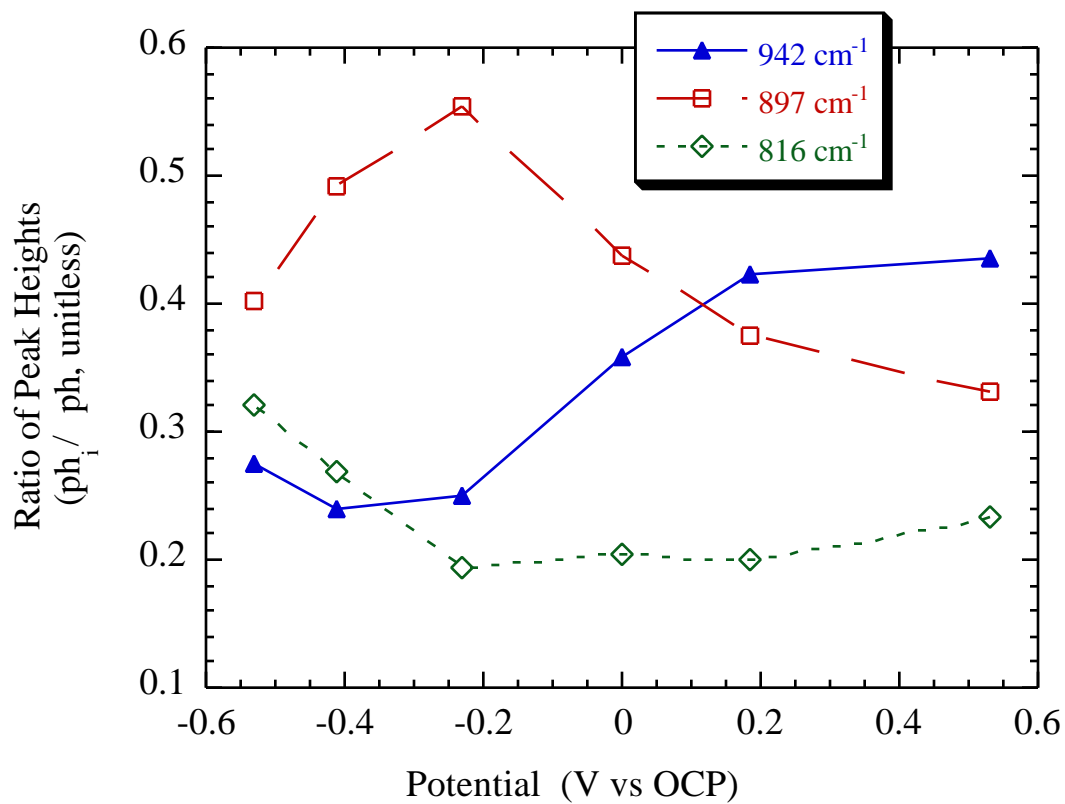


Figure 11 Ratio of the 942, 897, and 816 peak heights as a function of applied potential (vs the open circuit potential). The 816 and 942 cm^{-1} peaks are associated with WO_3 and $\text{WO}_3(\text{H}_2\text{O})_x$ respectively.

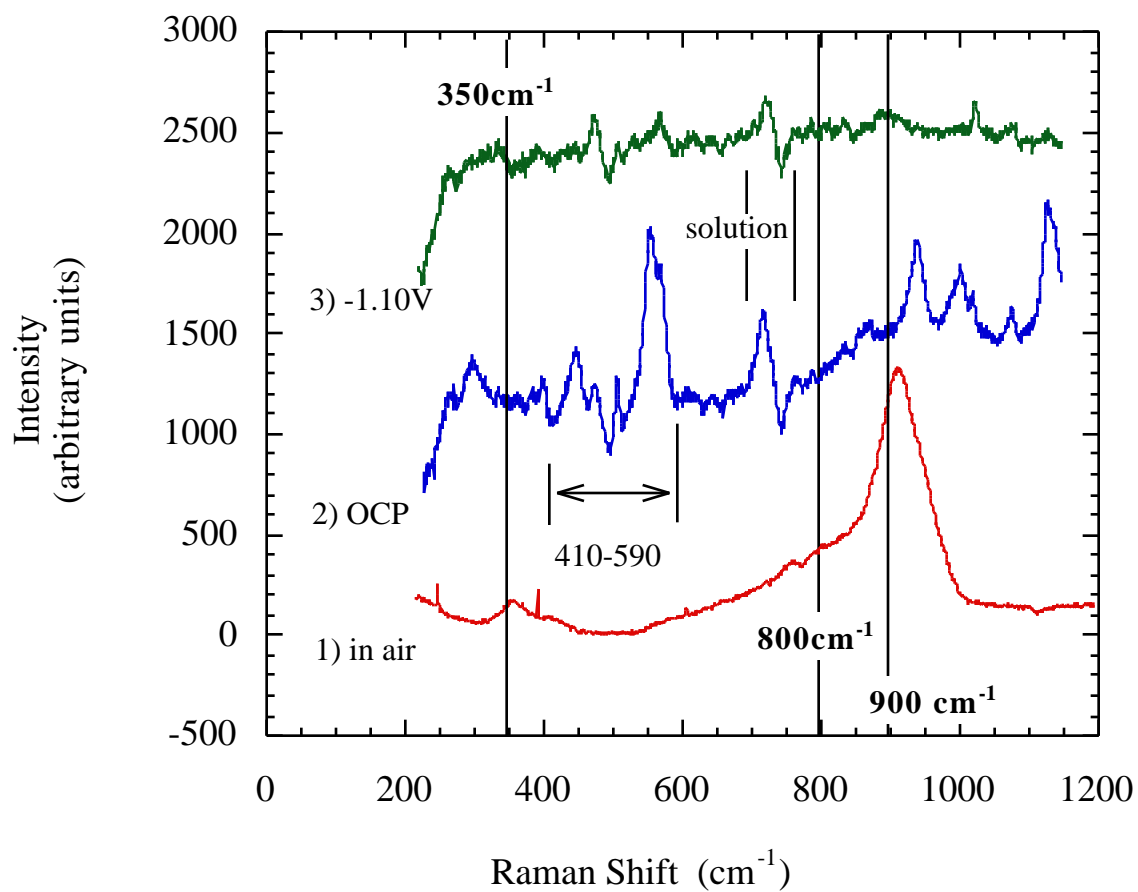


Figure 12 *In situ* SERS spectra of W as a function of potential. (pH 10.6). In-air spectrum is also presented for reference. The number of each curve represents the order of experiments.

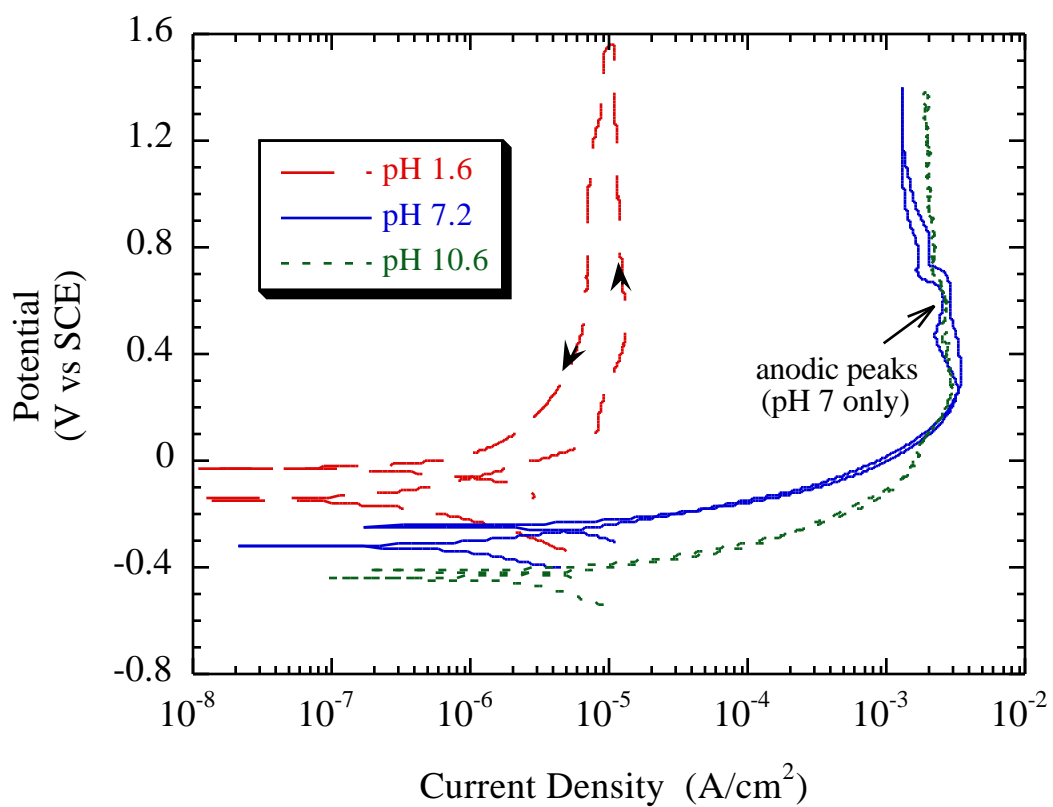


Figure 13 Potentiodynamic polarization curves for tungsten as a function of solution pH.

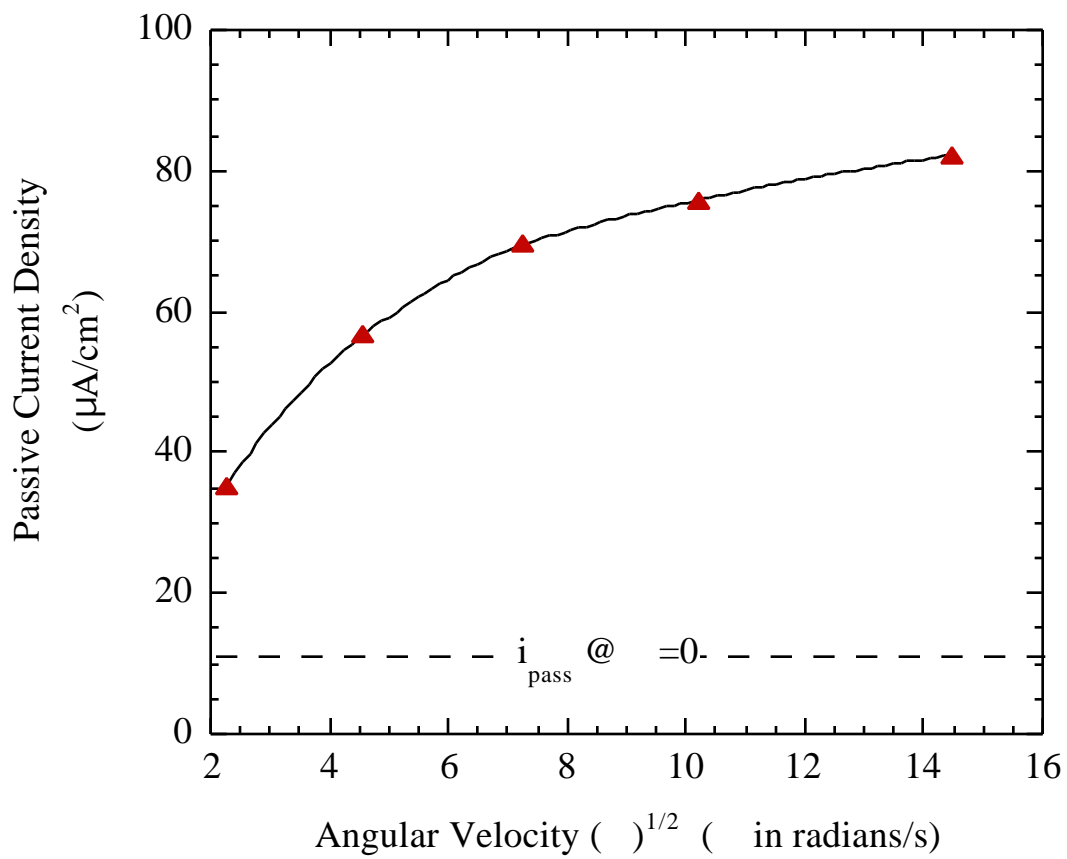


Figure 14 Effect of the angular velocity of the electrode on the W passive current density in H_2SO_4 , pH 1.6 at an applied potential of 0.20 V SCE.

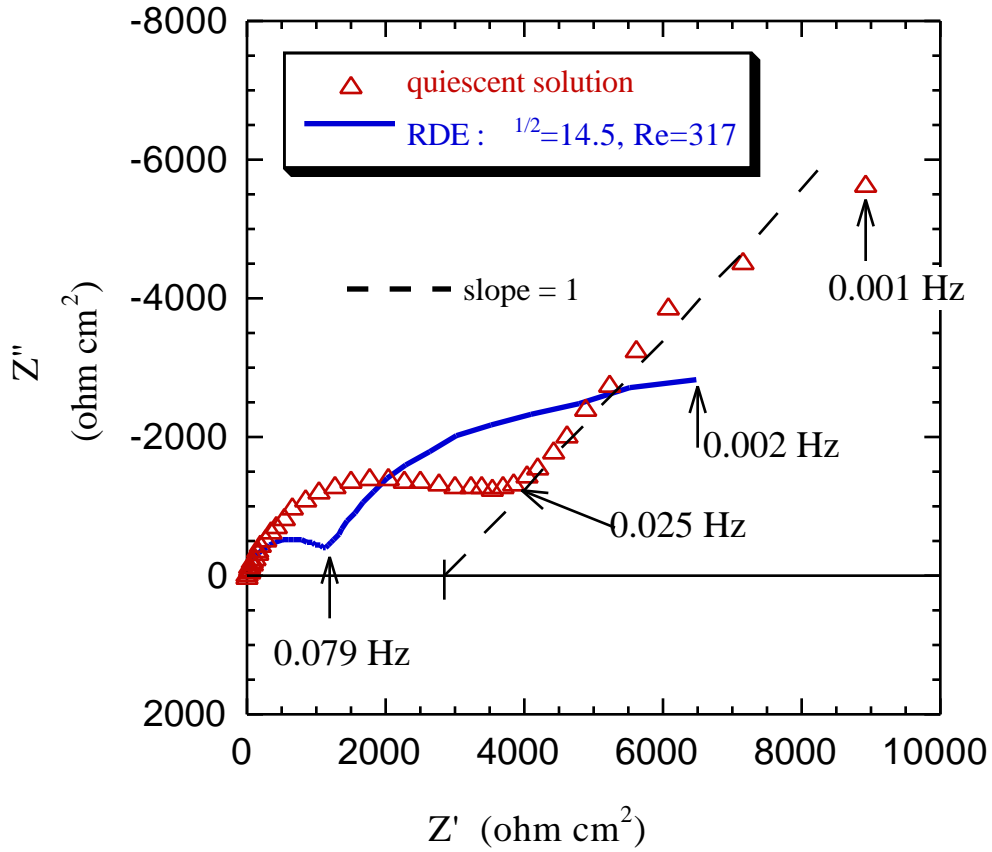


Figure 15 Nyquist plot for tungsten in H_2SO_4 , pH 1.6 showing the effect of rotation rate.

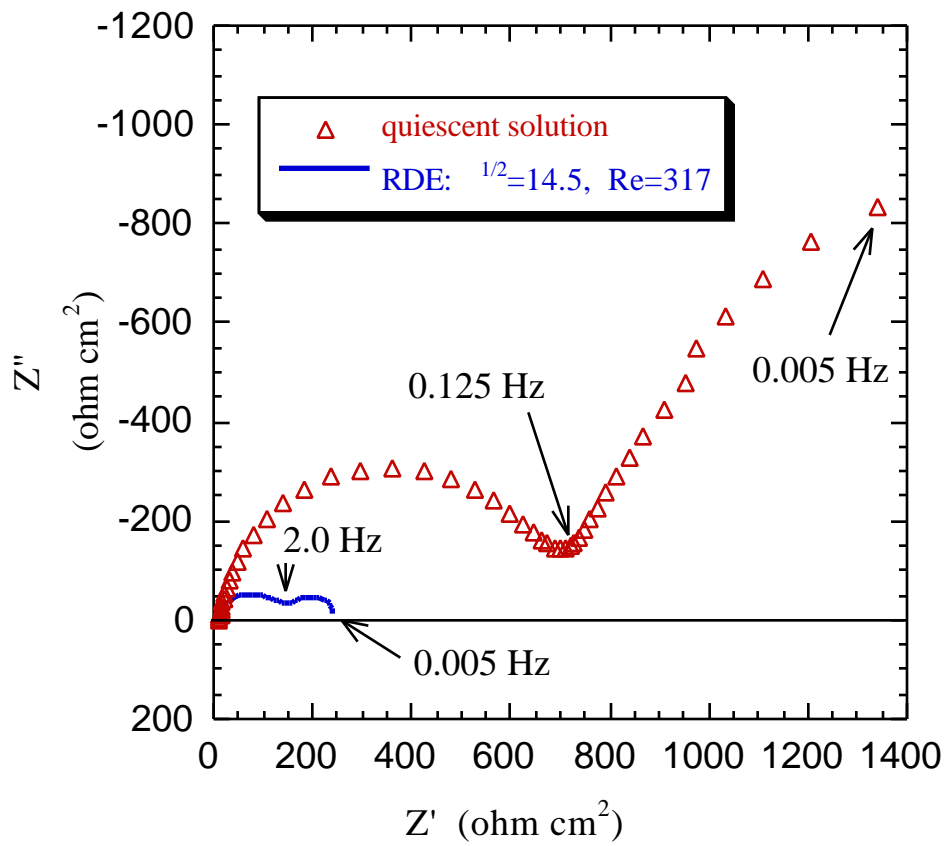


Figure 16 Nyquist plots for tungsten in borate buffer pH 7.2 showing the effect of rotation rate.

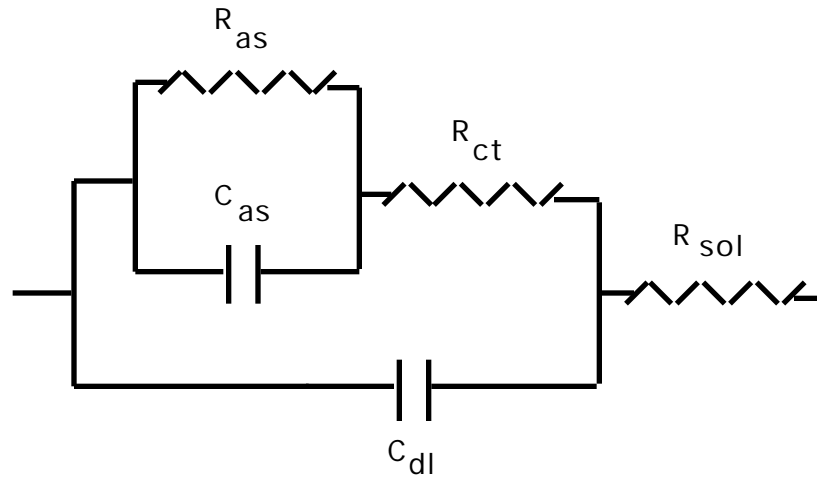


Figure 17 Equivalent circuit used to model tungsten EIS data, where: R_{sol} is the geometric resistance due to the solution, R_{ct} is the resistance associated with charge transfer, C_{dl} is the capacitance associated with the double layer, R_{as} is the impedance associated with the discharge of an adsorbed species, and C_{as} is the adsorption pseudocapacitance associated with the adsorbed species.

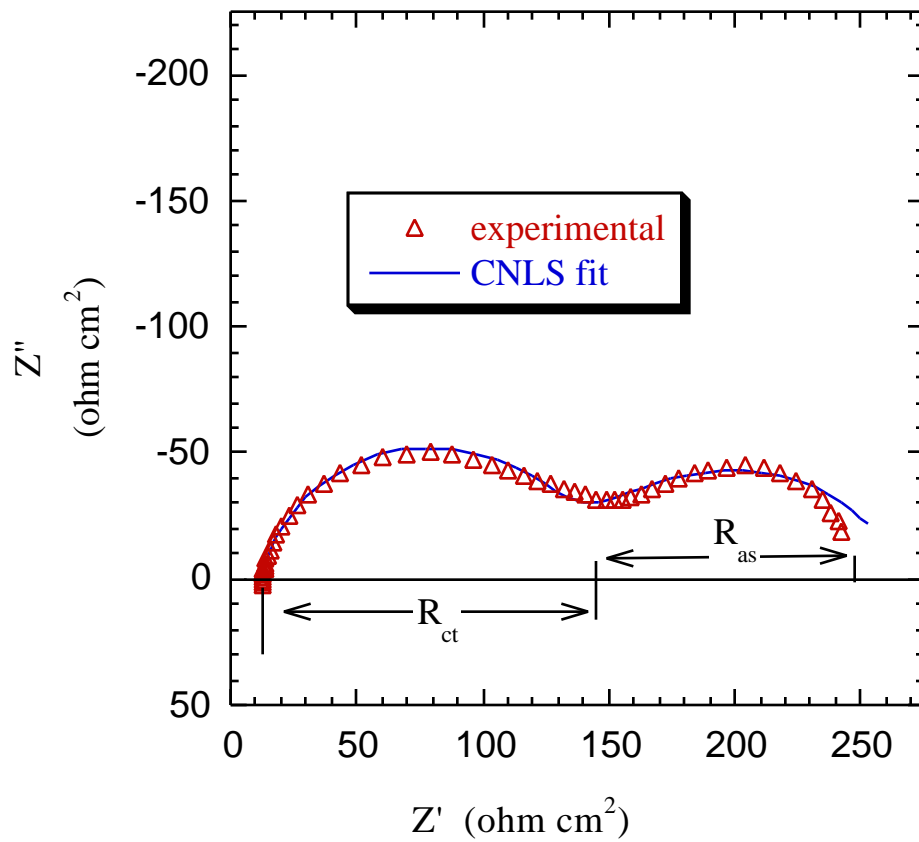


Figure 18 Nyquist plot for tungsten in pH 7.2 $\tau^{1/2} = 14.5$ and CNLS fit of the EC in Figure 17 to the data. Also shown are the X-intercepts of the some of parameters in the EC.